Materials Research. 2023; 26:e20230176
DOI: https://doi.org/10.1590/1980-5373-MR-2023-0176

Evaluation of Microstructural, Mechanical and Corrosion Behaviours of Laminated AA6061/AA7075 Metal Matrix Composites Build by Friction Stir Additive Manufacturing for Structural Applications

Sai Chand Kundurti[a] **,** ***Ambuj Sharma***[a]*

[a]*VIT-AP University, School of Mechanical Engineering, 522237, Andhra Pradesh, India*

Received: March 21, 2023; Revised: June 23, 2023; Accepted: July 29, 2023

The structural performance of metallic components is a significant challenge especially when it comes to operating conditions in real-world applications. Friction stir additive manufacturing (FSAM) is a solid-state additive manufacturing (AM) that provides controlled microstructure with homogenous grains and excellent structural performance. In this study, the FSAM technique was utilized to fabricate a lightweight laminated AA6061/AA7075 metal matrix composite with improved mechanical properties. The feasibility of the FSAM was demonstrated to build multi-functional, multi-material components for aerospace, automotive, and defence industries to enable lightweight, high-strength components. The FSAM tool was designed with an optimum shoulder length, shoulder diameter, pin length, and pin diameter considering the plate thickness. Afterward, optimized process parameters were designed using the Taguchi L9 orthogonal array (OA) technique. Microstructural features and their effect on mechanical properties such as microhardness and ultimate tensile strength (UTS) were evaluated in the FSAM build. FSAM build improved in microhardness (from 107±1.2 to 138.4 ±2.8 $HV_{0.2}$) and tensile strength (from 310 to 384 MPa) as compared to base material AA6061. Corrosion resistance was also studied to understand the feasibility of the FSAM technique in various environmental conditions. The overall performance of the FSAM build shows promising results compared to the base materials.

Keywords: *Friction stir additive manufacturing, Aluminum alloys, Taguchi technique, Microstructure, Microhardness, Corrosion resistance.*

1. Introduction

In recent years, lightweight metal matrix composites (MMCs) have been widely utilized for structural applications in all most all manufacturing sectors such as the defence industrial base sector, marine, automobile and aerospace sectors because of their excellent structural performance and durability[1]. The fabrication techniques significantly influence the microstructural grain features and mechanical properties of MMCs[2]. Additive manufacturing (AM) is one of the promising fabrication techniques that have emerged over recent years to fabricate multilayer structural components of metal[3]. AM has transformed significantly in recent decades and still progress needed to fully mature. This requires further research and development to address cost, standardization, quality, and material challenges[4-6]. Conventional AM techniques for metallic materials are employed liquid-solid transformation-based processing in which several challenges limit their industrial applications[7] such as (i) inhomogeneous microstructure[8], (ii) processing defects e.g., porosity, solidification-related defects[9], (iii) manufacturing volume, and manufacturing rate[10], (iv) cost of production[11]. To overcome these challenges, researchers have explored solid-state AM techniques which are capable of handling most of the above concerns[12-14]. FSAM is solid-state AM that provides controlled microstructure with homogenous grains and excellent structural performance[15-17].

Aluminum metal matrix composites (AMMCs) are mostly preferable for structural applications because of their lower density, excellent wear and corrosion resistance, and high formability[18]. Recyclability, the capacity to accept surface treatments, and durability are additional standout characteristics of aluminum that make it suitable for various engineering applications[19,20]. Several researchers have recently been interested in FSP to create an efficient surface composite for industrial applications[21]. Friction Stir Processing (FSP) was initially used for aluminum composites, but now it fabricates composites of various metals and polymers. It has also revolutionized the development of functionally graded metal matrix systems/surfaces[22]. Further, the friction stir engineering principles are adopted into AM techniques to build various surface MMCs. The first friction joining AM was patented by White in 2004[23]. The first report was published by Airbus in 2006 stating that additively manufactured components can be built by using the friction stir technology[24]. Airbus[24] and Boeing[25] also claimed that this technology can achieve maximum outputs at higher production rates with minimal wastage. FSAM technique is utilizing the friction stir welding (FSW) principle where stacks of metal sheet can be joined using a non-consumable rotating tool[26]. This solid-state AM technique aids in the production of an effective joint between the layers by the controlling process parameters of FSW,

*e-mail: sharma.ambuj@vitap.ac.in

especially tool rotational and traverse speed. Palanivel et al.[27] build magnesium alloy WE43 multistack through the FSAM method under different rotational and travel speeds to understand the microstructural and mechanical characteristics. This research established the role of heat input in the FSAM process to control the microstructure and eliminate the process defect by using Zener-Hollomon parameters. They observed controlled microstructure (2~3 μm) along with enhanced mechanical properties. Yuqing *et al.* studied the morphology and the mechanical performance of FSAM-built annealed multi-layered stacks made of AA7075. High ultimate strength and compromised ductility were reported for all layers in comparison to the base alloy. Microhardness dramatically improved in the build direction of the FSAM build component. They also pointed out that the hook defects and kissing defects formed from the second layer on the advancing side through the build direction[28]. Zhang et al.[29] studied the mechanical properties under the influence of re-stirring effect and the variable thermal cycles effect on the multilayer FSAM build of AA6061-T6 stack on AA6082 substrate. The finer grain sizes were found but the microhardness and tensile strength varied up to three layers of AA6061, whereas the addition of more layers did not show significant variations in the properties. Srivastava et al.[30] developed a 20 mm height component using Al5059/SiC of six layered stack using FSAM technique to study the microstructural and microhardness characteristics. The results revealed that an effective bonding between the subsequent layers with a finer grain sizes and higher microhardness as compared to the base material.

The FSAM technology is used in the present work to create novel laminated AMMCs for advanced structural applications. To get over the limitations of the traditional AM technique, the authors adopted the FSAM process. To the best of the knowledge of authors, so far limited studies carried out to build dissimilar aluminum alloys AA6061/AA7075 multilayer stack with one on top of the other. Contributing to the development of AM by expanding its capacity to create complex and customised structures, the authors use FSAM technology to investigate the building of different aluminium alloys in a layered stack. Research findings may lead to novel approaches for producing high-performance structural components that meet the needs of a wide range of industries. As the FSAM process is in the developing phase, there are no optimized process parameters to avoid manufacturing defects and achieve controlled microstructure throughout the FSAM build. In this work, an attempt has been made to optimize the process parameters using Taguchi L9 orthogonal array (OA) and ANOVA techniques. Microstructural and mechanical characterizations were carried out to determine the efficacy of the FSAM technology. The corrosion behaviours of multistack build in diverse environmental situations were also investigated to understand their applicability in a wide variety of applications.

2. Experimental Procedure

2.1. Optimization of process parameters for FSAM Technique

One of the effective ways to choose the best process variables for the intended outcome is through the Taguchi L9 OA methodology. In this study, the most influential parameters of the friction stir lap welding (FSLW) process like tool rotational speed (TRS); tool traverse speed (TTS); tool tilt angle (TTA) were considered and optimized for FSAM technique to build multi-layered stacks of AA6061/AA7075. The other process parameters like tool plunge depth, shoulder plunge depth, and tool pin profile are maintained constant throughout the process as these are the least influential process parameters when compared to the TRS, TTS and TTA parameters. The parameters were optimized by considering them in three levels (L1, L2 and L3), as shown in Table 1.

For the trial experiments, Taguchi L9 OA approach was used. Using a shear-cut machine, the 3 mm thick AA6061-T6/AA7075-T6 plates were cut into 200 x 100 mm dimensions. AA7075-T6 was placed on top of the AA6061-T6 during FSLW due to its higher hardness. Harder material can be flown easily into softer material. The straight threaded cylindrical profile tool made with H13 tool steel was used for FSLW of dissimilar materials[31,32]. The tool's profile has been designed according to the thickness of the plate[33]. Shank and shoulder diameters (ø) considered are 18 mm and 25 mm, whereas pin diameter (ø) and length were taken as 6 mm and 4.7 mm respectively. The lap welding was performed according to the set of parameters mentioned in Table 2. Hardness and % of elongation are considered as response variables for this analysis to understand the quality of weldments. On a Micro Vickers Hardness Tester, the microhardness of the welded specimens was assessed, and tensile tests were performed on a universal testing machine (UTM) to determine the % of elongation for all specimens. The average values of hardness and % of elongation were taken for L9 OA analysis. The test results of % elongation and Vickers hardness of all the sets of parameters are represented in Table 2.

The uncontrolled factors in an experiment were eliminated using the Signal to Noise (S/N) ratio in the ANOVA approach. To accomplish the desired outcome, three quality parameters were used: larger is better, smaller is better, and nominal is better. The maximum hardness and % elongation are

Table 1. Three levels of parameter optimization.

S. No.	Parameters	L1	L2	L3
1	TRS (rpm)	710	900	1120
2	TTS (mm/min)	40	50	63
3	TTA (in degrees)	1	2	3

Table 2. % Elongation and hardness results of all specimens.

TRS (rpm)	TTS (mm/min)	TTA (in degrees)	% Elongation	Hardness (Hv)
710	40	1	11.25	145.0
710	50	2	15.40	149.5
710	63	3	14.60	144.8
900	40	2	8.10	141.1
900	50	3	10.25	142.5
900	63	1	9.5	142.1
1120	40	3	11.90	143.5
1120	50	1	10.9	142.8
1120	63	1	9.25	140.4

important qualities for good weldments. Therefore, the larger the better characteristics were selected to calculate the S/N ratio to boost the response. The characteristics of the larger is better for S/N ratio is expressed as[34]:

$$S/N\ Ratio\ = -10\log\frac{1}{n}\cdot\Sigma\frac{1}{y^2} \tag{1}$$

where, y denotes the response variables of the i^{th} experiment and n denotes the number of experiments.

Table 3. represents the ANOVA results for % elongation of L9 OA sets of weldments. The percentage of contribution (PC) is computed by the ratio of sum of squares to total sum of squares as represented in Table 3. The significance of process parameters can be understood by PC, F value, and P-value. From Table 3, the higher F-value and lower P-value can be observed for rotational speed whereas low F-value and high P-value can be seen for TTS and TTA. The most significant contributor of the three process parameters is TRS which had the lowest P-value at 0.163 and the highest F-value and PC as 5.13 and 66.67% respectively. Also, it can be observed that TTS and TTA have lesser PC and F-value whereas higher P-value. It demonstrates that these two parameters are less significant for % elongation.

The response table for S/N ratio (larger the better) for % elongation is shown in Table 4. Larger S/N ratio represents optimal process parameters form the set of experiments. According to the table, the highest S/N ratios for TRS, TTS, and TTA are found in levels 1, 2, and 3 respectively. The higher mean of S/N ratios represents the optimal process parameters out of the selected range of parameters. As a result, TTA of 3^0 degrees; the TRS 710 rpm; and TTS 50 mm/min were best process parameters for achieving effective elongation and as a result excellent weldability was obtained.

Table 5. depicts the response of ANOVA for hardness of the weldments. From Table 5, the highest F-value and the lowest P-value were obtained for the rotational speed yields the highest PC 35.95% whereas PC for TTS and TTA were slightly lower 24.64% and 20.10%. Therefore, the hardness of the weldments was majorly influenced by TRS followed by TTS and TTA.

The good weldments should have higher hardness to resist penetration. Therefore, the larger the better-quality characteristics have chosen for S/N ratio for hardness which is shown in Table 6. According to the table, the highest S/N ratios for TRS, TTS, and TTA are found in levels 1, 2, and 3 respectively. So, it can be concluded that a TTA of 3^0 degrees; the TRS 710 rpm; and TTS 50 mm/min were the best process parameters for achieving effective hardness and, as a result, excellent weldability was obtained.

Based on the hardness and % of elongation ANOVA data, it can be determined that the ideal welding parameters for AA6061/AA7075 stack are TRS of 710 rpm; a TTS of 50 mm/min; and a TTA of 3^0 degrees.

2.2. Fabrication of laminated AA6061-T6/AA7075-T6 AMMC using FSAM technique

In this research, AA6061-T6 and AA7075-T6 aluminum sheets were taken as base materials to build a multistack through the FSAM technique. The dimensions of the bottom plate used for the FSAM build was in the dimensions of 150 mm length, 130 mm width and 6.35 mm thickness, whereas the other plates used for stacking up on this base plate were in dimensions of 150 mm length, 130 mm width and 3 mm thickness. The chemical compositions and mechanical properties of the AA6061-T6 and AA7075-T6 are shown in Table 7 and Table 8, respectively, as provided by the material supplier in a data sheet[35].

FSAM is a repeating FSLW technique that joins metal sheets one over the other in the layered manner[36]. In this experiment, hmt milling machine was used for performing the FSAM process. Various kinds of clamping setups were utilized to hold the specimens tightly to withstand the higher loads which results in effective control of the work pieces to reduce process defects. The flat threaded cylindrical tool pin profile was used to produce defect-free FSAM builds. This tool profile ensures a smooth material flow during welding with no major flaws. H13 tool steel was used to fabricate the FSAM tool with dimensions: shoulder Φ25 mm; shank Φ18 mm; pin Φ6 mm; pin length of 4.7 mm; as shown in Figure 1. The Taguchi L9 OA and ANOVA methodologies

Table 3. ANOVA results for % elongation.

Source	DF	Sum of Squares	Mean sum of squares	F-value	P-value	Percentage of Contribution (P.C)
TRS	2	31.316	15.658	5.13	0.163	66.67%
TTS	2	4.749	2.374	0.78	0.563	10.11%
TTA	2	4.802	2.401	0.79	0.560	10.22%
Error	2	6.107	3.054			
Total	8	46.974				

Table 4. % Elongation response table.

Levels	TRS	TTS	TTA
1	**13.750**	10.417	10.550
2	9.283	**12.183**	10.917
3	10.683	11.117	**12.250**
Delta	4.467	1.767	1.700
Rank	1	2	3

Table 5. ANOVA results for hardness.

Source	DF	Sum of Squares	Mean sum of squares	F-value	P-value	Percentage of Contribution (P.C)
TRS	2	23.21	11.604	1.86	0.349	35.95%
TTS	2	15.91	7.954	1.28	0.439	24.64%
TTA	2	12.98	6.488	1.04	0.490	20.10%
Error	2	12.47	6.234			
Total	8	64.56				

Table 6. Hardness response table.

Level	TRS	TTS	TTA
1	**146.4**	143.4	143.3
2	142.5	**146.3**	144.0
3	144.4	143.6	**146.1**
Delta	3.9	2.9	2.8
Rank	1	2	3

Table 7. Chemical composition of AA6061-T6 and AA7075-T6 alloys used in the study[35].

Materials	Mg	Cu	Zn	Cr	Fe	Mn	Si	Ti	Al
AA6061-T6	1.05	0.20	0.03	0.09	0.45	0.18	0.62	0.07	Balance
AA7075-T6	2.64	1.49	5.68	0.21	0.16	0.03	0.03	0.048	Balance

Table 8. Mechanical properties of AA6061-T6 and AA7075-T6 alloys used in the study.

Material	Yield Strength (YS) (MPa)	Ultimate Tensile Strength (UTS) (MPa)	Elongation (%)	Hardness (Hv)
AA6061-T6	276	310	17	107
AA7075-T6	503	572	11	175

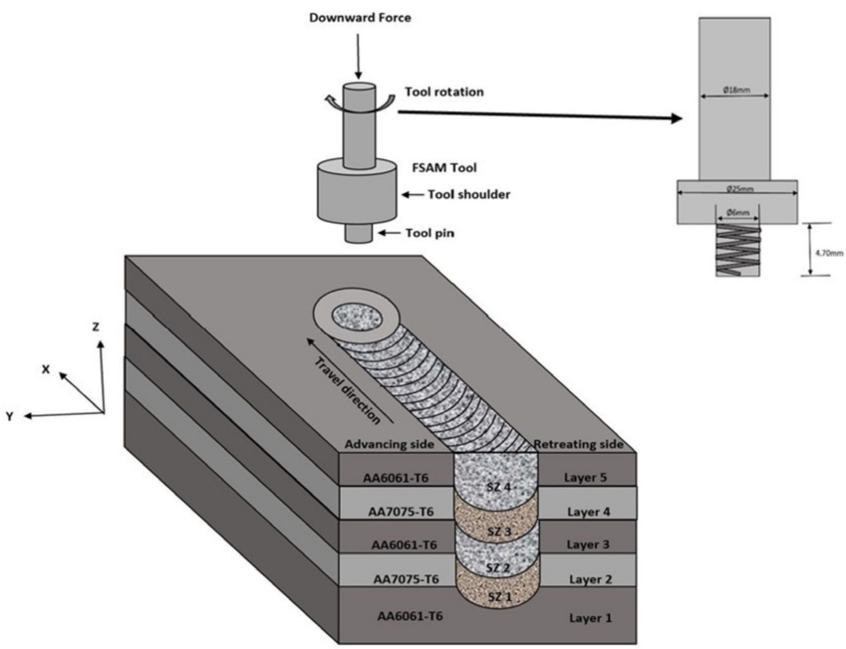

Figure 1. Schematic representation of FSAM procedure along with the tool for FSAM.

were used to optimize the process parameters (TRS of 710 rpm, TTS of 50 mm/min, and TTA of 3^0 degrees) for the multistack plates. Throughout the procedure, 4.7 mm of tool pin plunge depth and 0.1 mm of shoulder plunge depth were held constant. Aluminum alloy sheets were initially positioned on the machine bed in a lap position and suitably secured without any gaps between the plates. After that, the revolving FSAM tool was moved forward for 140 mm. FSAM process was carried out in a single pass for every layer laid on top of the other layer. These steps were repeated four times to achieve 5-layer FSAM build with 18 mm height as shown in Figure 1. As the FSAM stack consists of five layers made up of AA6061-T6 and AA7075-T6 alloys stacked one on top of the other, AA6061-T6 is referred to as 6 and AA7075-T6 is referred to as 7, and the overall stack is referred to as 6-7-6-7-6 stack from here on throughout. Further Figure 2. represents the way the test samples are extracted from the total FSAM build specimen for various characterizations namely for microstructural, mechanical, and corrosion behaviour. For evaluating the reliability of the results, each test was repeated twice, and the average of the test results was taken into consideration for all the test specimens throughout the experimentation. Appropriate care was taken while extracting the samples from the FSAM build specimen using wire-cut EDM machine.

2.3. Specimen preparation for characterizations

2.3.1. Microstructural analysis

The Metallographic test samples were made based on the ASTM E3-95 method[37]. Samples of size 35 mm x 18 mm x 10 mm were taken out from FSAM build using a wire-cut EDM machine. The polishing of the samples for morphological analysis was done using different grades of emery sheets (150 to 3000 μm) to remove the scratches[38]. In addition, the samples were mirror polished with the diamond paste of 0.25 μm before being etched using Keller's reagent (2.5 ml HNO_3, 1.5 ml HCl, 1 ml HF, and 95 ml H_2O) to analyse the macro and micro features of the samples. The microstructures of the interfacial layers and different zones of FSAM build were characterized using OLYMPUS MODEL-BX53M metallurgical microscope. The elemental composition and microstructures of the different layers of FSAM specimens were seen using a JCM-6000 plus Scanning Electron Microscopy (SEM) with Energy Dispersive Spectroscopy (EDS)[39]. SZ of the FSAM build was extracted for X-ray diffraction (XRD) analysis[40].

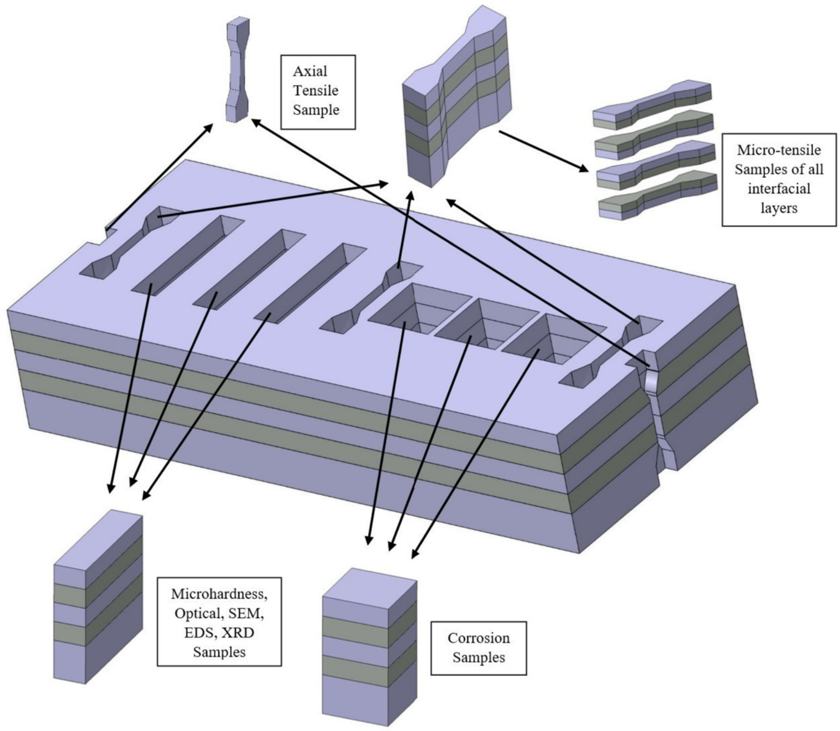

Figure 2. Samples extracted from FSAM build.

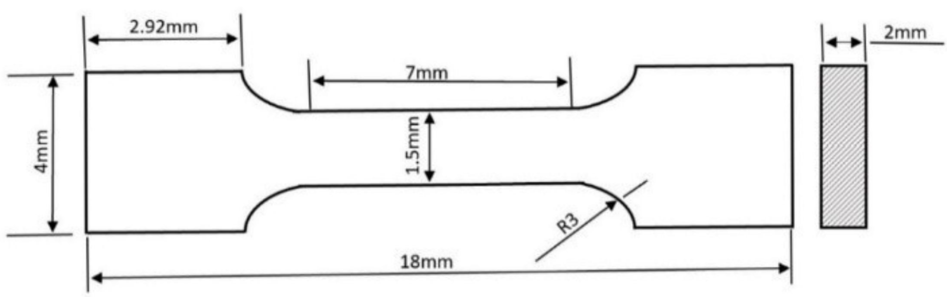

Figure 3. Micro-tensile sample dimensions.

The MiniFlex Benchtop X-ray Diffractometer from Rigaku Americas Corporation was used to study the FSAM cross-sectioned sample. During XRD, the scanning speed rate at which the diffractometer moved during the measurement was considered as 10° per minute, the 2θ, the scattering angle was considered to the range of 90° and the incident radiation angle was considered as 3°. These adjustments aimed to achieve optimal data quality and enable accurate diffraction pattern analysis for the current research study.

2.3.2. Mechanical analysis

The mechanical properties of specimens were evaluated to understand the structural performance of the FSAM build. The UTS and YS of the samples were determined using a 10 kN capacity universal testing equipment (H10KL). The standard micro tensile specimens were made in accordance with ASTM WK49229[41] as shown in Figure 3. The test was conducted at an ambient temperature with a strain rate of 1 mm/min. The fractography analysis was conducted using SEM to understand the behaviour of fracture surfaces. Microhardness tests were conducted using a square pyramid-type diamond indenter to examine the hardness variation in all layers through the vertical (build) and horizontal directions, carried out on the Vickers Hardness Tester (METCO-VH-LMDX)[42,43]. A 200 g load was released and applied slowly through the indenter for 10 seconds on the specimen surface to measure microhardness across the specimens at different zones.

2.3.3 Corrosion analysis

The corrosion analysis of the base alloy and the FSAM build sample were studied by using the Tafel polarization curves plotted at room temperature as per the ASM standard using a PARSTAT 2273 apparatus[44]. To conduct the corrosion test, the samples were extracted from the parent alloy and SZ of the FSAM sample with a uniform square cross section of 1 cm^2 by wire-cut EDM. The samples were then polished with 1200 grit emery paper and further cleaned with alcohol and water to avoid any foreign particles that stick on top of the surface. Thus, the samples were then put into the container having an aqueous solution containing 3.5 wt% NaCl. After mounting, polishing, and re-establishing electrical contact, all specimens were employed as working electrodes and held for 30 minutes to achieve balance before introducing current into the circuit. Platinum (counter electrode) and calomel (reference electrode) electrodes were used to complete the electrochemical circuit[45]. After reaching the steady-state condition, the initial and final potentials in the open circuit potential (OCP) were kept at -0.25 mV and +0.75 mV. The Tafel plots were obtained at a scan rate of 1mVs^{-1} [46].

3. Results and Discussion

This section demonstrates the examination of FSAM build microstructural characteristics, corrosion behaviour, and mechanical properties. Micrographs are obtained from an optical microscope and SEM analysis. Elemental compositions were confirmed from EDS analysis. XRD analysis was also performed to check the crystallinity and dislocation density of the build specimen. Mechanical behaviour and corrosion resistance qualities were thoroughly studied to assess the structural performance of multistack FSAM build.

3.1. Microstructural analysis

Microstructural analysis of FSAM build was a little complicated as it consists of different layers of friction stir lap welds which were subjected to different temperatures while stacking up one layer over the other. Temperature raised due to pin stirring was distributed from top stack to bottom stack thought out the process yield annealing effects on subsequent layers. The final build microstructure is completely dependent on the initial base aluminum alloy microstructure. The base materials AA6061-T6 and AA7075-T6 microstructures are shown in Figure 4a, b reveal the grains are coarser and banded arranged in the direction of rolling.

The optical macrograph of FSAM build is shown in Figure 5a. The proper stirring throughout the build from bottom to top can be observed in the macrograph. The macrograph image shows that there were no wormholes appeared especially in the SZ which means that the adapted optimum process parameters for FSAM enabled the effective mixing of dissimilar materials to form an effective metallurgical bonding between the layers. There were no visible defects in all the interfacial joints of the build. In this fabrication process, the tool stirs deep into the bottom layer and the shoulder gets in contact with the top layer allowing the material to stir effectively to build a joint between the two layers. Thus, the total joint was divided into three zones namely Stir Zone (SZ) where the tool dwells into the two layers, Thermo-Mechanically Affected Zone (TMAZ) where the shoulder gets in contact and helps the material subjected to both the heat effect as well as the stirring effect and lastly Heat Affected Zone (HAZ) closer to the TMAZ where the area just subjected to the heat alone. The microstructures and grain sizes of these three zones can show the efficacy of the FSAM process.

Different regions are marked on the macrograph as represented in Figure 5a to understand the process effects on the microstructural characteristics of build. Region 1 is considered at TMAZ/HAZ zone of interfacial joint 1 at advancing side (AS). HAZ zone of interfacial layer 2 is taken as region 2 at AS. SZ/TMAZ of the middle of layer 3 at retreating side (RS) is considered as region 3. Regions 4 and 5 are taken at the SZ of the interfacial layers 3 and 4 respectively. Regions 1, 2 and 3 are considered for the optical microscopic analysis while regions 4 and 5 are considered for SEM and EDS analysis. The interfacial layers are critical in defining the overall build quality of the FSAM components since the FSAM build was subjected to various stirring actions and temperature distribution along the build zone. As a result, in this work, the interfacial layers are subjected to microstructural and grain size analysis to assess the overall build quality of the FSAMed multistack plate. Micrographs obtained from regions 1, 2 and 3 are shown in Figure 4b-d. From these micrographs, it can be observed there was a uniform mixing of dissimilar alloy materials and no major process defects such as hook defects, kiss bonding, micropores, or major voids and tunnel defects in

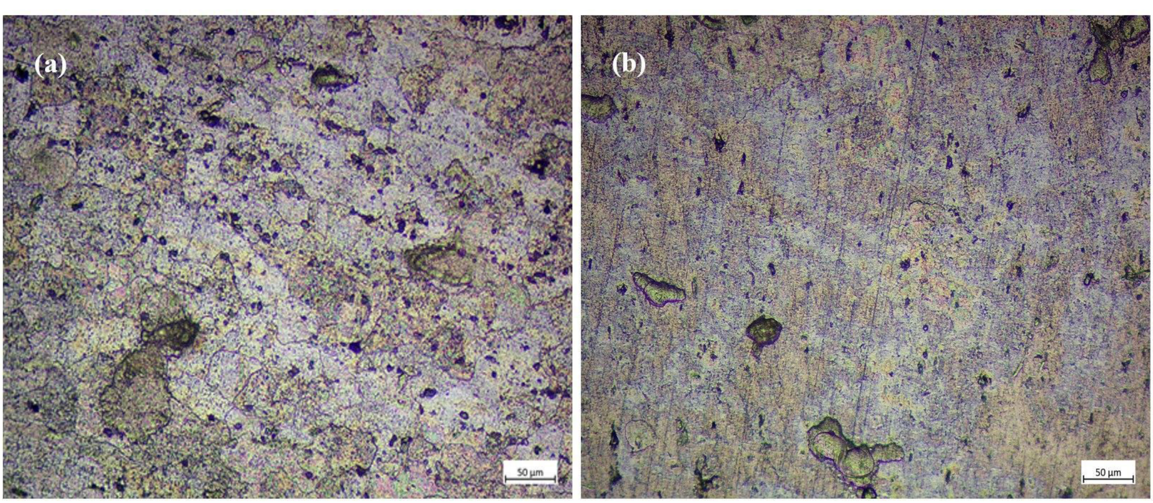

Figure 4. Optical micrographs: (a) AA6061-T6, (b) AA7075-T6.

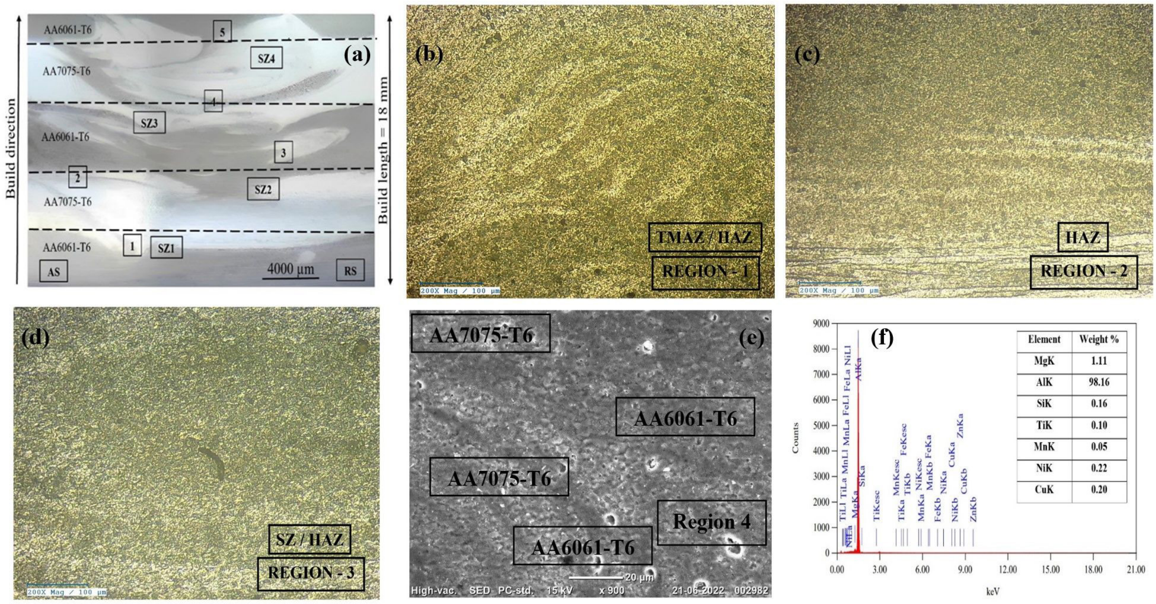

Figure 5. (a) Macrograph of FSAM multi-layered build cross-section, (b-d) optical micrographs of build cross-section at various locations represented in macrograph,(e) SEM image of SZ at interfacial layer 3 (region 4 in macrograph), (f) EDS elemental mapping results at region 5 in macrograph.

different zones of the joints[47]. The stirring action performed by the tool and the temperature developed in the SZ helps the dynamic recrystallization which dominates the annealing and helps in forming the refined grains that can be observed in Figure 5b-d as compared to the BM. During the FSAM process material stacks were subjected to different temperature cycles, strain rates which results in an effective dynamic recrystallization, coarsening and refinement of grains which occurs simultaneously. Initially, the grains of the material were subjected to the stirring action and temperature which helps them to form into coarser grains[35]. Subsequently, due to the increase in strain rates, the newly elongated coarser grains divide into finer grains.

Figure 5e depicts the SEM morphology of region 4. Usually, the material having higher atomic numbers appear brighter in the SEM micrographs. Similarly, Figure 5e shows the brighter portions which resemble the AA7075-T6, and darker portions resemble the AA6061-T6 alloys mixing in an appropriate manner. Also, proper intermixing of materials at SZ with a ring pattern, indicating strong interfacial adhesion was observed. EDS elemental mapping has been carried out at interfacial layer 4 (region 5), shown in Figure 5f. The findings of the EDS elemental mapping demonstrate the presence of Al and other major alloying elements like Mg, Si, Ti, Mn, Ni, Cu etc. Oxidizing elements were not detected in EDS elemental analysis which establish the proper joining of materials without porosity.

Table 9. represents the grain refinement of FSAM build at various locations as compared to BM. From the Table 9, it is clearly observed higher grains refinement in the SZ as compared to TMAZ, HAZ and BM. Less refined grains were noticed in TMAZ as compared to SZ because it was less subjected to thermal and mechanical actions. The elongated grains were noticed in the HAZ region due to thermal effect without much strain rate. Likewise, it was

Table 9. Grain sizes of BM and FSAM build at interfacial layers in the build direction.

Location	Maximum Grain Size (µm)	Minimum Grain Size (µm)	Average Grain Size (µm)
AA6061-T6 BM	97.6	54.7	84.2
AA7075-T6 BM	86.6	47.9	68.4
Interfacial layer-1 SZ	15.8	1.32	4.8
Interfacial layer-1 TMAZ	21.1	5.6	8.9
Interfacial layer-1 HAZ	26.7	10.1	14.6
Interfacial layer-2 SZ	13.9	0.98	3.4
Interfacial layer-2 TMAZ	20.8	4.7	7.8
Interfacial layer-2 HAZ	25.3	9.2	13.9
Interfacial layer-3 SZ	11.7	0.76	2.7
Interfacial layer-3 TMAZ	19.7	4.9	6.8
Interfacial layer-3 HAZ	23.2	8.7	12.7
Interfacial layer-4 SZ	10.6	0.55	1.9
Interfacial layer-4 TMAZ	17.3	3.2	5.4
Interfacial layer-4 HAZ	21.7	5.4	10.3

observed for all the interfacial layers from bottom to top (1 to 4) where grains were less refined in the interfacial layer-1 and refinement increased gradually in subsequent layers in the build direction due to different heat cycles and annealing effects during FSAM process.

The XRD peaks observed for the 6-7-6-7-6 build are plotted in Figure 6a. Furthermore, XRD peaks are compared to JCPDS data, and observed all significant peaks are matched, as shown in Figure 6b. Also, full-width half maxima (FWHM) and all different peak positions (2h) are evaluated and then the following equations are used to compute crystallite size (C_s), dislocation density (Φ_d), and micro-strain (ε_s): (2-4).

$$C_S = \frac{K\, x\, \lambda}{\beta_t \cos\theta} \tag{2}$$

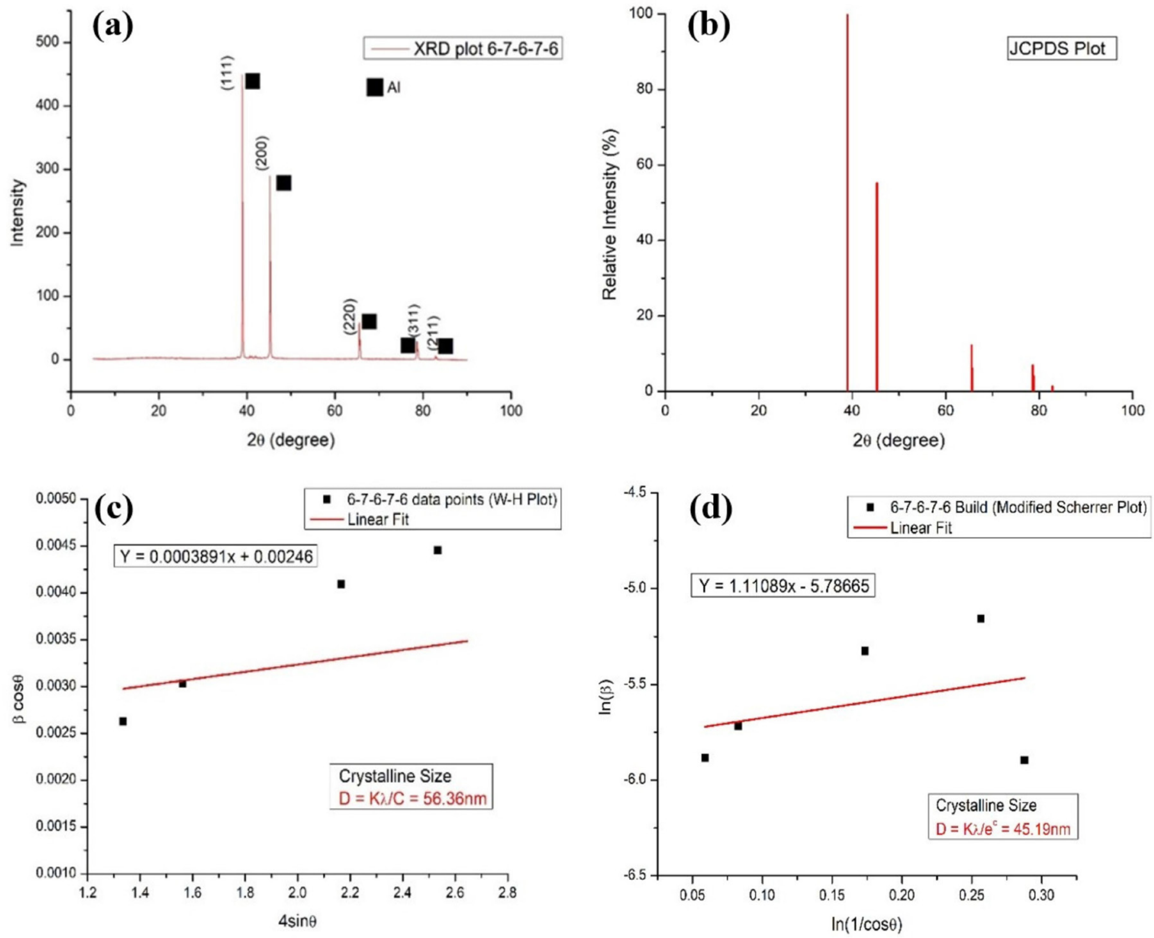

Figure 6. (a) XRD graph, (b) JCPDS graph, (c) W-H graph, (d) Modified Scherrer graph.

$$\Phi_d = \frac{1}{{C_s}^2} \tag{3}$$

$$\varepsilon_s = \frac{\beta_t}{4\tan\theta} \tag{4}$$

where, K = shape factor (taken as 0.9), λ = wavelength of X-ray (0.15406 nm), β_t = full width half maxima (FWHM), θ = peak positions (in radians).

FWHM (βt), the crystallite size (C_s), the dislocation density (Φ_d), and the micro-strain (ε_s) of various XRD peaks are shown in Table 10.

The Williamson-Hall (W-H) plot (Figure 6c) was derived by using the Scherrer equation:

$$\beta_t \cos\theta = \varepsilon_s\left(4\sin\theta\right) + \frac{K\lambda}{C_s} \tag{5}$$

The plot shown in Figure 6c is drawn by straight-line fitting the data points noted from the XRD data by considering 4sinθ on the x-axis and β_t cosθ on the y-axis. The W-H plot reveals that the C_s is 56.36 nm. A modified-Scherrer (m-S) plot (shown in Figure 6d) is constructed using the following equation:

Table 10. FWHM (β_t), the crystallite size (C_s), the dislocation density (Φ_d), and the micro-strain (ε_s) of various XRD peaks.

Peak Position (2θ)	β_t (in degrees)	C_s(nm)	Φ_d X $(10)^{-3}$	ε_s x $(10)^{-3}$
39.00593	0.159598298	52.81	0.36	1.97
45.97148	0.18867927	45.74	0.48	1.94
65.54516	0.278747001	33.89	0.87	1.89
78.62127	0.330198474	31.01	1.04	1.76
82.82286	0.157384815	67.03	0.22	0.78

$$ln\,\beta_t = ln\left(\frac{1}{cos\,\theta}\right) + ln\left(\frac{K\lambda}{C_s}\right) \tag{6}$$

The C_s is evaluated from the m-S plot is 45.19 nm, which is exactly in between the analytical and W-H plot findings.

3.2. Mechanical analysis

Tensile testing was conducted to evaluate the strength of all interfacial layers and in the build direction of the FSAM sample. Weldments strength is compared to BM AA6061-T6 and AA7075-T6. The UTS of the AA6061-T6 and AA7075-T6 was noted 310 MPa and 572 MPa, respectively. Tensile test results of all interfacial layers in the build direction and axial tensile sample are shown in Table 11. The weldments exhibited good strength and almost retained 60-80% of the base material AA7075-T6. The ultimate tensile strength (UTS) of interfacial layers (1-4) from bottom to top were 294 MPa, 322 MPa, 363 MPa, and 384 MPa respectively. UTS of axial tensile sample was 376 MPa. It is noted that the YS and UTS of all the interfacial layers gradually increased from bottom to the top due to the grain's refinement and annealing effect[37,38]. A similar trend for the yield strength of the interfacial layers can be observed in Table 11. The percentage elongation of interfacial layer weldments was 10-20% lower than the base alloys as represented in Figure 7.

The mechanical action of the rotating tool during the process causes the material to undergo severe plastic deformation, leading to dynamic recrystallization and the formation of smaller grains. The reduction in grain size is beneficial as it generally leads to improved mechanical properties, such as increased strength and enhanced ductility. The mechanical properties of these layers are expected to fall between the properties of the two base alloys due to the blending of their respective microstructures and compositions. Since the grain size was significantly reduced during the process, the resulting interfacial layers are likely to exhibit improved mechanical properties compared to the base alloys, although they may not match the properties of either alloy precisely. The observation of increasing strength from the bottom to the top of the interfacial layers suggests a possible variation in microstructure or composition along the joint. The observed gradual increase in strength from the bottom to the top of the layers may be attributed to variations in the intensity of plastic deformation and heat input during the process.

The fractography analysis was carried out to understand the fracture behaviours of all tensile samples of interfacial layers in the build direction, as shown in Figure 8a-d. Different sizes and shapes of dimples along with varied tearing edge thicknesses are observed from the images. On all the samples, the necking phenomenon is observed which reveals decent plastic deformation before fracture. It can be also observed that the voids are comparatively reduced in the direction of build from interfacial layers 1 to 4. Interestingly, the tear edges along the grain boundaries are continuously improved in the build direction from bottom to top (interfacial layers 1 to 4), which can be noticed in the fracture images. These observations indicate an improvement in the strength and elongation along the build direction, as noticed in Table 11. Also, all the tensile fractures showed a ductile mode of failure which means that the FSAM build has an effective interfacial bonding between the layers due to the effective mixing of the material in between the dissimilar alloy layers[29].

Figure 9. depicts the schematic of the 6-7-6-7-6 build cross-section and microhardness measurements. Microhardness tests in the build direction of SZ, AS, and RS are marked in three vertical lines in Figure 9, and respective results are displayed in Figure 10. Microhardness variations in the build direction can be noticed in this Figure 10. The horizontal microhardness measurements on layers (1-5) from AS to RS are indicated in Figure 9, and the corresponding hardness is plotted in Figure 11. The microhardness varies

Table 11. Tensile properties of FSAM sample at different interfacial layers.

Specimen	UTS (MPa)	Yield Strength (MPa)	Strain (%)	Fracture location centre	Fracture mode
AA6061-T6 BM	310	276	17	Centre of gauge length	Ductile
AA7075-T6 BM	572	503	11	Centre of gauge length	Ductile
Interfacial layer - 1	294	264	10.5	HAZ Weld	Ductile
Interfacial layer – 2	322	298	9.56	HAZ Weld	Ductile
Interfacial layer – 3	363	340	8.8	HAZ Weld	Ductile
Interfacial layer – 4	384	344	8.22	HAZ Weld	Ductile
Axial Tensile Sample	376	360	8.6	Centre of gauge length	Ductile

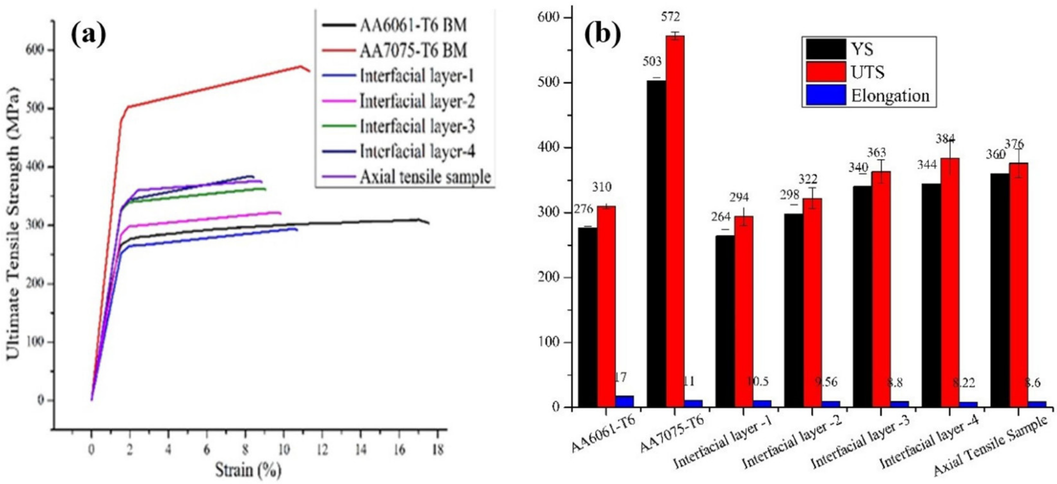

Figure 7. Comparison of tensile test of BM and FSAM build samples.

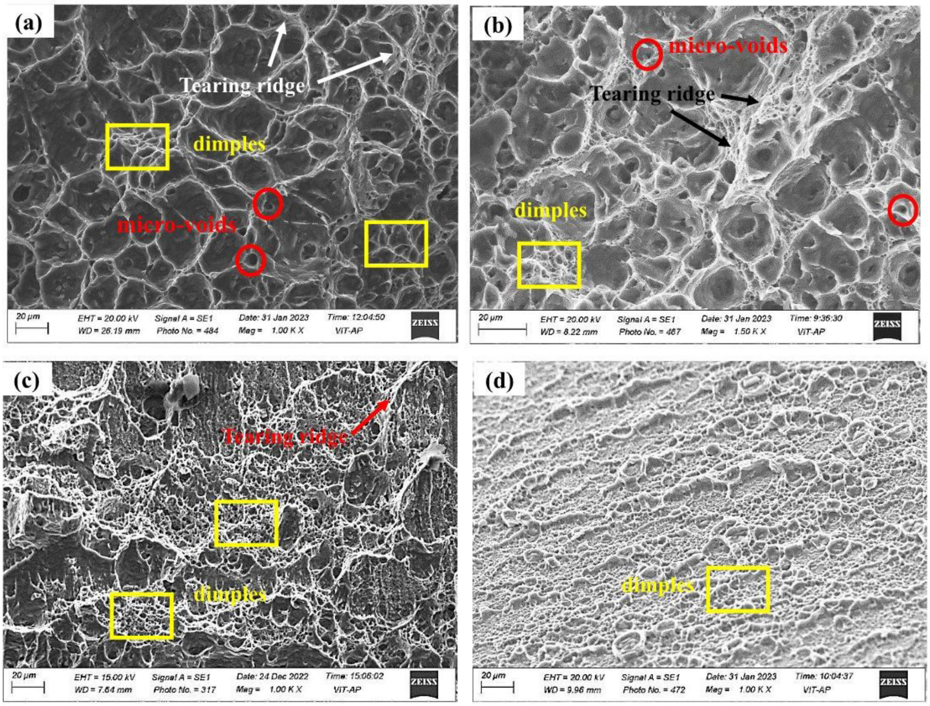

Figure 8. Fractographies of all interfacial layer tensile samples in FSAM build direction: (a) interfacial layer-1, (b) interfacial layer-2, (c) interfacial layer-3, (d) interfacial layer-4.

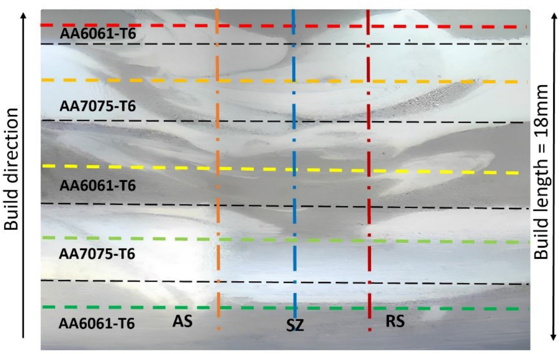

Figure 9. Microhardness testing locations of FSAM sample.

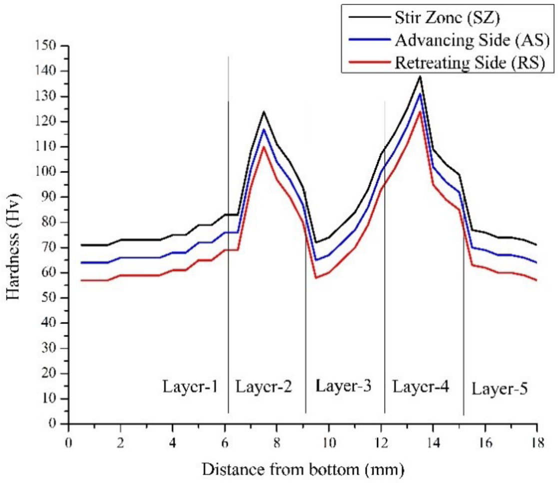

Figure 10. Microhardness in vertical build direction in WZ, RS, and AS.

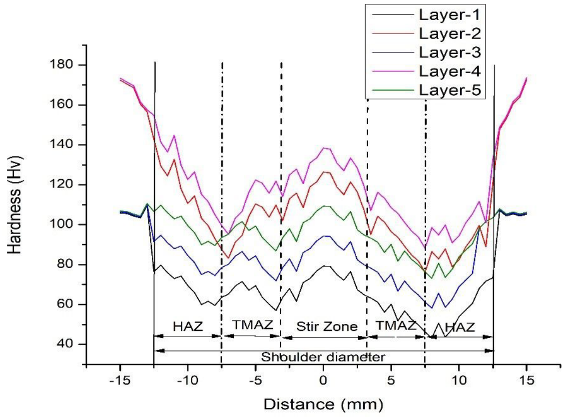

Figure 11. Microhardness in the horizontal direction for all layers in the build direction.

across distinct layers of the FSAM build. SZ microhardness measurements demonstrate significant improvement when compared to HAZ and TMAZ along all the five layers of the FSAM build can be observed in Figure 11. The SZ of layer 4 has the highest hardness of 138.4 Hv. This increase in SZ's micro hardness might be because of higher plastic deformation and grain refinement that occurred during mechanical stirring and simultaneously thermal shocks cause dynamic recrystallizations, which occur primarily at the interfacial layers where the fine-grained microstructure was observed. It is also worth noting that the manufactured FSAM build's RS has a lower hardness due to grain formation in HAZ because of the annealing action. The lowest hardness of 43.2 Hv was observed at the HAZ of layer 1. The difference in microhardness is observed due to the microstructure variations across the build direction owing to the existence of a varying thermal cycles during the fabrication.

3.3. Corrosion analysis

The corrosion behaviour of BM and FSAM samples was evaluated through the potentiodynamic polarization test by employing a conventional 3-electrode cell. The electrochemical setup includes a calomel electrode (CE) as a reference electrode, samples for testing as a working electrode, and platinum as a counter electrode. Before the electrochemical test, the samples are submerged in a 3.5% NaCl solution for around 30 minutes at room temperature until a steady state open circuit voltage (E_{corr}) is obtained. The scanning rate was kept at 1 mv/s to conduct the polarization test. The exposed surface area of the samples of the solution is 1 cm^2. The anodic and cathodic curves were explored for corrosion potentials to evaluate the corrosion resistance using the Tafel plot. I_{corr} is evaluated with the E_{corr} using the following Stern-Gearvy Equation 7

$$I_{corr} = \left(\frac{\beta_a \times \beta_b}{2.303 \cdot R_p \left(\beta_a + \beta_b \right)} \right) \tag{7}$$

The corrosion rate (CR) is calculated as:

$$Corrosion\ Rate = 3.27 * 10^{-3} I_{corr} * \left(Ew / \rho \right) \tag{8}$$

Where 3270 is constant, Ew is the equivalent weight (gms), and ρ is the density (g/cm^3).

The electrochemical responses in the form of anodic reaction of aluminum alloys in a natural environment containing chloride as:

$$Al + 3H_2O.\ Al\left(OH\right)_3 + 3H^+ + 3e^- \tag{9}$$

As the alloy's pitting potential corresponds to its resting potential, pit formation causes aluminum dissolution, which causes chloride ions to migrate into the pit where the aluminum chloride is produced as:

$$Al.\ Al^{+3} + 3e^- \tag{10}$$

$$Al^{+3} + 3Cl^- AlCl_3 \tag{11}$$

The electrochemical procedure described below, on the other hand, is proposed for aluminum cathodic polarization:

$$O_2 + 2H_2O + 4e^- 4OH^- \tag{12}$$

$$2H_2O + 2e^- 2OH^- + H_2 \tag{13}$$

Figure 12. shows a parent alloy's typical Tafel polarization curves and the FSAM build top surface of SZ. Pitting behaviour was detected in the FSAM sample from the anodic side as shown in Figure 13. Corrosion resistance was slightly lower for the FSAM build as compared to the parent alloy due to reheating effect throughout the fabrication of the build. Finer grains formed in the SZ are slightly higher corrosion susceptible, which may be related to higher grain boundary density causing the increase in total surface reactivity than the parent alloy.

Table 12. shows that the E_{corr} of the parent alloy was about -710 mV vs. CE, whereas that of the FSAM build sample was around -660 mV vs. CE. Furthermore, the I_{corr} for the parent alloy was -1.74 Acm^{-2} compared to -1.79 Acm^{-2} for the FSAM build sample. The value of corrosion rate is inversely proportional to corrosion resistance, whereas pitting potential (E_{pit}) is directly proportional to corrosion resistance. It is observed that FSAM build shows a slightly different corrosion rate and low pitting potential, leading to minutely low corrosion resistance with respect to parent alloy.

Figure 13. shows a micrograph of the surface of the FSAM build sample following a polarization test. Localized

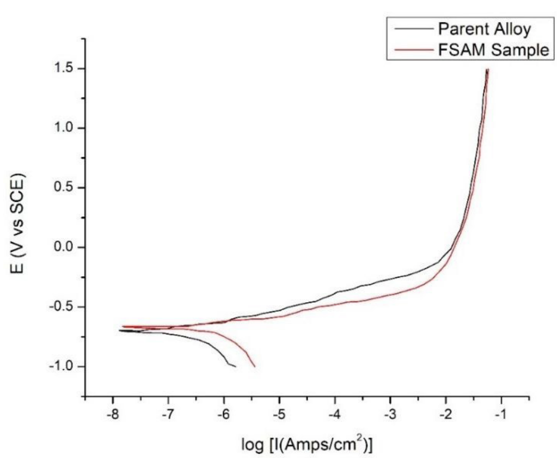

Figure 12. Parent Alloy and FSAM build sample Tafel polarization curves.

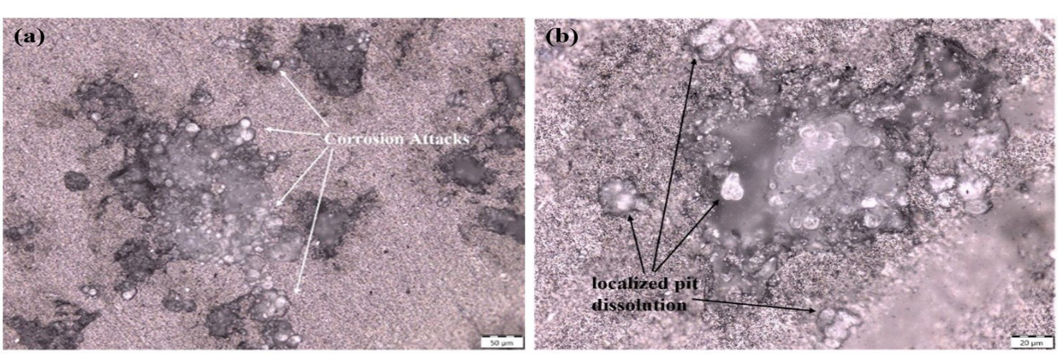

Figure 13. Optical micrograph examination of FSAM build sample surface after corrosion test.

Table 12. Parent alloy and FSAM build sample Tafel polarization test results.

Material/ Process	E_{corr} (V)	I_{corr} (mA)	E_{pit} (V)	Corrosion rate (mm.y^{-1})
Parent Alloy	-0.71	-1.73	-0.65	0.019126433
FSAM Build Sample	-0.66	-1.79	-0.63	0.019727789

corrosion pits are clearly visible in Figure 13. Localized pit dissolution with intergranular corrosion is identified in the micrograph as a major corrosion type in the FSAM build sample. The localized pit dissolution along with extensive intergranular corrosion was found slightly higher in the FSAM build sample as compared to the parent alloy. The high temperature during the joining process is the primary source of alterations in the FSAM build sample's microstructure. Repeated thermal shocks in the SZ, impacts the chemistry of the grain boundaries, sensitizing the grain boundary region significantly in comparison to the parent alloy leading to the lower corrosion resistance of the FSAM sample.

4. Conclusions

By using optimal process settings, a 5-layered 6061-T6/7075-T6 FSAM build was successfully fabricated. The present investigation's key results are listed below:

i. FSAM is a novel solid-state AM method that may be used to produce structural components with a completely gradient microstructure in the most cost-effective manner.

ii. When the OM and SEM analysis were performed, the refined grain structures were detected in the SZ of the fabricated build. Furthermore, the major problems encountered in fusion-based AM methods can be addressed by attaining the controlled microstructures utilizing FSAM.

iii. The 5-layered 6-7-6-7-6 build component has higher tensile strength in the interfacial layers than the base AA6061-T6, but lower than the base AA7075-T6, due to the homogeneous mixing of two different alloy materials in all interfacial layers. Furthermore, the SZ of all interfacial layers has a greater microhardness than the TMAZ and HAZ across the construction cross-section. The SZ of top interface (interfacial layer 4) had the maximum microhardness of 138.4 Hv, while the lowest hardness of 43.2 Hv was found in the bottom layer of the HAZ interface on the RS of the build.

iv. Intermetallic phases were confirmed through XRD analysis which may be one of the reasons for the improvement in hardness of the FSAM build. In the SZ of FSAM build, the analytical values for crystallite size (C_s), micro-strain (ε_s), and dislocation density (Φ_d) were 52.81 nm, 0.36×10^{-3} nm^2, and 1.97×10^{-3}, respectively. The W-H plot and m-S plot both reveal that the crystallite size (C_s) is approaching the analytical value.

v. The FSAM build shows a slightly variable corrosion rate and low pitting potential which ultimately leads to minutely lower corrosion resistance when compared to the parent alloy due to the smaller grains formation during the mechanical stirring and thermal treatment throughout the build.

FSAM process is in the initial stage of its development. Improvising these kinds of AM techniques will enable industries to adopt them to manufacture complicated structural components in an easier manner. By using this AM technology, industries can replace all the heavy metal body structural components with lightweight materials with equivalent mechanical properties enabling an increase in efficiency. However, there are many challenges that to be resolved in the FSAM technique to adopt as an alternative method in the current AM technologies and ways to use it for mass production which ultimately helps the goal of industrial revolution 4.0 to produce the complex parts with low cost of production.

5. Acknowledgments

The work was supported by the VIT-AP University, Amaravati.

6. References

1. Garg P, Jamwal A, Kumar D, Sadasivuni KK, Hussain CM, Gupta P. Advance research progresses in aluminium matrix composites: manufacturing & applications. J Mater Res Technol. 2019;8(5):4924-39.
2. Sharma A, Singh S, Pal K. Investigation of microstructural and mechanical properties of Al alloy 7075-T6/B4C nanocomposite concocted via friction stir process. Ceram Int. 2022;48(23):35708-18.
3. Zhang WN, Wang LZ, Feng ZX, Chen YM. Research progress on selective laser melting (SLM) of magnesium alloys: a review. Optik (Stuttg). 2020;207:163842.
4. Srivastava M, Rathee S. Additive manufacturing: recent trends, applications and future outlooks. Prog Addit Manuf. 2022;7(2):261-87.
5. Palanivel S, Mishra RS. Building without melting: a short review of friction-based additive manufacturing techniques. International Journal of Additive and Subtractive Materials Manufacturing. 2017;1(1):82-103.
6. Rathee S, Srivastava M, Maheshwari S, Kundra TK, Siddiquee AN. Friction based additive manufacturing technologies: principles for building in solid state, benefits, limitations, and applications. Boca Raton: CRC Press; 2018.
7. Parwani AK, Ramkumar PL, Abhishek K, Yadav SK. Recent advances in mechanical infrastructure. USA: Springer Singapore; 2020.
8. Zhang LC, Liu Y, Li S, Hao Y. Additive manufacturing of titanium alloys by electron beam melting: a review. Adv Eng Mater. 2018;20(5):1700842.
9. Zhang J, Song B, Wei Q, Bourell D, Shi Y. A review of selective laser melting of aluminum alloys: processing, microstructure, property and developing trends. J Mater Sci Technol. 2019;35(2):270-84.
10. Bournias-Varotsis A, Han X, Harris RA, Engstrøm DS. Ultrasonic additive manufacturing using feedstock with build-in circuitry for 3D metal embedded electronics. Addit Manuf. 2019;29:100799.
11. Pérez M, Carou D, Rubio EM, Teti R. Current advances in additive manufacturing. Procedia CIRP. 2020;88:439-44.
12. Puleo SM. Additive friction stir manufacturing of 7055 aluminum alloy [thesis]. New Orleans: University of New Orleans; 2016.
13. Khodabakhshi F, Gerlich AP. Potentials and strategies of solid-state additive friction-stir manufacturing technology: a critical review. J Manuf Process. 2018;36:77-92.

14. Griffiths RJ, Perry ME, Sietins JM, Zhu Y, Hardwick N, Cox CD, et al. A perspective on solid-state additive manufacturing of aluminum matrix composites using MELD. J Mater Eng Perform. 2019;28:648-56.
15. Palanivel S, Nelaturu P, Glass B, Mishra RS. Friction stir additive manufacturing for high structural performance through microstructural control in an Mg based WE43 alloy. Materials & Design (1980-2015). 2015;65:934-52.
16. Palanivel S, Mishra RS. Building without melting: a short review of friction-based additive manufacturing techniques. International Journal of Additive and Subtractive Materials Manufacturing. 2017;1(1):82-103.
17. Perry ME, Griffiths RJ, Garcia D, Sietins JM, Zhu Y, Hang ZY. Morphological and microstructural investigation of the non-planar interface formed in solid-state metal additive manufacturing by additive friction stir deposition. Addit Manuf. 2020;35:101293.
18. Heidarzadeh A, Javidani M, Mofarrehi M, Farzaneh A, Chen XG. Submerged dissimilar friction stir welding of AA6061 and AA7075 aluminum alloys: microstructure characterization and mechanical property. Metals (Basel). 2021;11(10):1592.
19. Rambabu PP, Eswara Prasad N, Kutumbarao VV, Wanhill RJ. Aluminium alloys for aerospace applications. In: Prasad N, Wanhill R, editors. Aerospace materials and material technologies. Singapore: Springer; 2017; p. 29-52. (Indian Institute of Metals Series; 1).
20. Li H, Yan W, Li Z, Mariusz B, Senkara J, Zhang Y. Numerical and experimental study of the hot cracking phenomena in 6061/7075 dissimilar aluminum alloy resistance spot welding. J Manuf Process. 2022;77:794-808.
21. Kundurti SC, Sharma A, Tambe P, Kumar A. Fabrication of surface metal matrix composites for structural applications using friction stir processing–A review. Mater Today Proc. 2022;56:1468-77.
22. Rathee S, Maheshwari S, Siddiquee AN, Srivastava M. A review of recent progress in solid state fabrication of composites and functionally graded systems via friction stir processing. Crit Rev Solid State Mater Sci. 2018;43(4):334-66.
23. White D. inventor; Solidica Inc, assignee. Object consolidation employing friction joining. United States patent US 6,457,629. 2002.
24. Lequeu PH, Muzzolini R, Ehrstrom JC, Bron F, Maziarz R. High-performance friction stir welded structures using advanced alloys. In: AeroMat Conference; 2006 Jun; Seattle. Proceedings. Seattle.
25. Baumann JA. Production of Energy Efficient Preform Structures (PEEPS). Arlington, Virgínia, EUA: The Boeing Company; 2012.
26. Chen Y, Cai Z, Ding H, Zhang F. The evolution of the nugget zone for dissimilar AA6061/AA7075 joints fabricated via multiple-pass friction stir welding. Metals (Basel). 2021;11(10):1506.
27. Palanivel S, Sidhar H, Mishra RS. Friction stir additive manufacturing: route to high structural performance. JOM. 2015;67:616-21.
28. Yuqing M, Liming K, Chunping H, Fencheng L, Qiang L. Formation characteristic, microstructure, and mechanical performances of aluminum-based components by friction stir additive manufacturing. Int J Adv Manuf Technol. 2016;83:1637-47.
29. Zhang Z, Tan ZJ, Li JY, Zu YF, Liu WW, Sha JJ. Experimental and numerical studies of re-stirring and re-heating effects on mechanical properties in friction stir additive manufacturing. Int J Adv Manuf Technol. 2019;104:767-84.
30. Srivastava M, Rathee S. Microstructural and microhardness study on fabrication of Al 5059/SiC composite component via a novel route of friction stir additive manufacturing. Mater Today Proc. 2021;39:1775-80.
31. Ilangovan M, Boopathy SR, Balasubramanian V. Effect of tool pin profile on microstructure and tensile properties of friction stir welded dissimilar AA 6061–AA 5086 aluminium alloy joints. Def Technol. 2015;11(2):174-84.
32. Garg A, Raturi M, Bhattacharya A. Influence of additional heating in friction stir welding of dissimilar aluminum alloys with different tool pin profiles. Int J Adv Manuf Technol. 2019;105:155-75.
33. Wronska A, Andres J, Altamer T, Dudek A, Ulewicz R. Effect of tool pin length on microstructure and mechanical strength of the FSW joints of Al 7075 metal sheets. Commun - Sci Lett Univ Zilina. 2019;21(3):40-7.
34. Devaiah D, Kishore K, Laxminarayana P. Optimal FSW process parameters for dissimilar aluminium alloys (AA5083 and AA6061) using taguchi technique. Mater Today Proc. 2018;5(2):4607-14.
35. KUMZ: Kamensk-Uralsky Metallurgical Works J.S.Co. Chemical composition of AA6061-T6 and AA7075-T6 alloys; 1; Mallinath Metal: No. 21/3, Sanghvi Sadan. 4th ed. Mumbai, Maharashtra, India: Near Alankar Cinema.
36. Srivastava AK, Kumar N, Dixit AR. Friction stir additive manufacturing–An innovative tool to enhance mechanical and microstructural properties. Mater Sci Eng B. 2021;263:114832.
37. ASTM: American Society for Testing and Materials. ASTM E3-95-Standard Practice for Preparation of Metallographic Specimens. West Conshohocken: ASTM; 1995.
38. Jha KK, Kesharwani R, Imam M. Microstructural and micro-hardness study on the fabricated Al 5083-O/6061-T6/7075-T6 gradient composite component via a novel route of friction stir additive manufacturing. Mater Today Proc. 2022;56:819-25.
39. Jha KK, Kesharwani R, Imam M. Microstructure and mechanical properties correlation of FSAM employed AA5083/AA7075 Joints. Trans Indian Inst Met. 2023;76(2):323-33.
40. Srivastava M, Rathee S, Maheshwari S, Noor Siddiquee A, Kundra TK. A review on recent progress in solid state friction based metal additive manufacturing: friction stir additive techniques. Crit Rev Solid State Mater Sci. 2019;44(5):345-77.
41. ASTM: American Society for Testing and Materials. WK49229 AS. New Guide for Orientation and Location Dependence Mechanical Properties for Metal Additive Manufacturing. West Conshohocken (PA): ASTM International; 2015. Work in Progress.
42. Sinha A, Farhat Z. Effect of surface porosity on tribological properties of sintered pure Al and Al 6061. Mater Sci Appl. 2015;6:549-66.
43. ASTM: American Society for Testing and Materials. ASTM E92-17. Standard test methods for Vickers hardness and Knoop hardness of metallic materials. West Conshohocken (PA): ASTM International; 2017.
44. Elatharasan G, Kumar VS. Corrosion analysis of friction stir-welded AA 7075 aluminium alloy. Strojniški vestnik- Jixie Gongcheng Xuebao. 2014;60(1):29-34.
45. Gharavi F, Matori KA, Yunus R, Othman NK. Corrosion behavior of friction stir welded lap joints of AA6061-T6 aluminum alloy. Mater Res. 2014;17:672-81.
46. Zhu M, Zhao BZ, Yuan YF, Guo SY, Pan J. Effect of solution temperature on the corrosion behavior of 6061-T6 aluminum alloy in NaCl solution. J Mater Eng Perform. 2020;29:4725-32.
47. Cole EG, Fehrenbacher A, Duffie NA, Zinn MR, Pfefferkorn FE, Ferrier NJ. Weld temperature effects during friction stir welding of dissimilar aluminum alloys 6061-t6 and 7075-t6. Int J Adv Manuf Technol. 2014;71:643-52.